Article

Simulation of Unconventional Resonator Cavity Geometries for a Novel and Efficient Microwave-Based Heating Method in False-Twist Texturing

Mathias Ortega [1,*], Ruitao Shi [1], Lukas Balon [1], Lars Musiol [2], Victor Bechthold [3], Roman Funk [3], Tobias Münstermann [4], Thomas Ramakers [4], Annegret Storm [1], Sven Ingebrandt [5], and Thomas Gries [1]

[1] ITA Institut für Textiltechnik of RWTH Aachen University, Otto-Blumenthal-Str. 1, 52074 Aachen, Germany;

[2] Fricke und Mallah Microwave Technology GmbH, Werner-Nordmeyer-Str. 25, 31226 Peine, Germany;

[3] Heimann Sensor GmbH, Maria-Reiche-Str. 1, 01109 Dresden, Germany;

[4] Barmag ZNL der Barmag GmbH & Co. KG, Leverkuser Str. 65, 42897 Remscheid, Germany;

[5] Institute of Materials in Electrical Engineering 1 of RWTH Aachen University, Otto-Blumenthal-Str. 6, 52074 Aachen, Germany

***** Corresponding author: Mathias Ortega. ORCID: 0000-0001-7027-7185

for engrXiv (Engineering Archive) on July 15th, 2026

Abstract

Melt-spun man-made fibres are crucial for the ever-rising demand for fibres. To use them in clothing or home textiles, they need the feel and properties of natural fibres, often imparted through texturing processes. The most dominant process, with 30 Mio. t production capacity per year, uses false-twist texturing to smooth melt-spun partially oriented yarns (POY) into crimped, fluffy draw-textured yarns (DTY). However, the heaters used in the process are long and inefficient, thereby compromising production efficiency. Short, efficient microwave heaters are proposed to overcome these drawbacks, reducing energy consumption by 40 % and increasing productivity by 20 %, leading to significant cost savings and equivalent CO_2 reductions during DTY production. However, conventional microwaves do not reach peak electric field strengths needed to heat the yarns in such a short residence time. Therefore, an optimisation algorithm is developed that couples a Genetic Algorithm and a high-frequency simulation to identify an unconventional microwave resonator geometry with high electric field strengths along the yarn path of polymeric multifilament yarns. First results show promising process behaviour and industrial yarn qualities. Future work will quantify energy efficiency and validate on a pilot scale along with a novel yarn temperature sensor.

Keywords: false-twist texturing; microwave heating; energy efficiency; DTY; optimisation

1. Introduction

Due to steadily increasing demand, more and more fibres need to be produced efficiently (**Figure 1**). Man-made fibres make up the majority of these fibres with 75 % market share. 79 % of those polymeric fibres are made using polyester (PET). Considering worldwide filament yarn production, PET has an even greater market share of 86 %, making it the single most important feedstock for man-made fibres. [1]

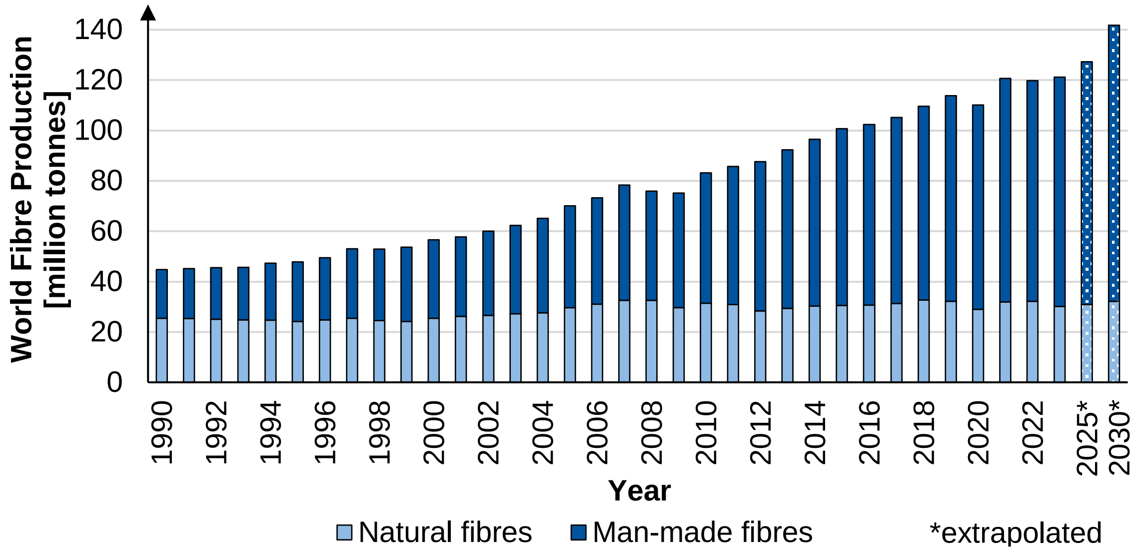

Figure 1: Importance of man-made fibre production in the world market. Created by the authors based on [1,2].

Smooth polymeric filaments are primarily employed in technical applications. To facilitate their use in apparel such as outerwear, sportswear, activewear, lingerie, hosiery, and stockings, home textiles such as carpets, upholstery, curtains, drapes, and bedding, or even technical textiles such as seats and headliners for automotive applications, yarns undergo a texturing process. There are different techniques for texturing. These include air jet texturing, knit-de-knit texturing, stuffer-box texturing, edge crimping, and false-twist texturing (FTT). Most of these techniques are already obsolete and have not changed in recent years. Partially oriented yarn (POY) is of significant importance for texturing. POY is predominantly drawn and crimped via false-twist texturing to produce draw-textured Yarn (DTY) [3,4]. As POY accounts for 60 % of globally manufactured melt-spun filament yarn, FTT – with an estimated 76-90 % market share and an annual output of approximately 30 million tonnes of DTY – represents the most significant texturing method within the textile industry. In total, approx. 25 % of all fibres are DTY. [1,2,5–9] During the production of DTY, crimp is imparted to each filament in the yarn (**Figure 2**), thereby providing a natural-fibre-like feel and appearance with greater elasticity, higher volume, better moisture absorption, dullness and improved comfort. This allows them to be used either independently or blended with natural fibres like cotton or wool, while maintaining strength, durability, quick drying, and moisture wicking in yarns and fabrics. [3,5,10,11] The dullness is caused by a change in the cross-sectional shape of the filaments. Round POY filaments become hexagonal DTY filaments during the extremely close packing of the filaments in the yarn compound during twist insertion in FTT, as can be seen in **Figure 2**. [12,13]

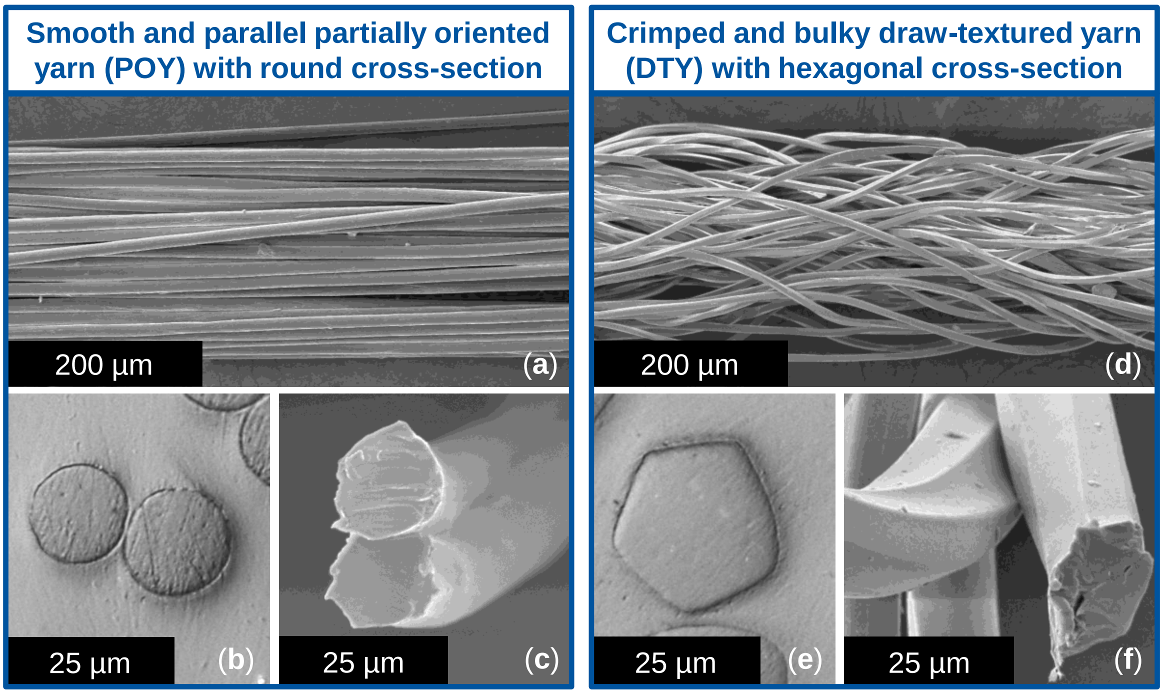

Figure 2: (**a**) SEM of flat partially oriented yarn (POY); (**b**) Light microscopy of round POY cross-section; (**c**) SEM of round POY cross-section (slightly smeared due to cutting); (**d**) SEM of crimped draw-textured yarn (DTY); (**e**) Light microscopy of hexagonal DTY cross-section; (**f**) SEM of hexagonal DTY cross-section.

False-twist texturing, also called false-twist draw-texturing or draw texturing, is a technique used to give synthetic yarns a natural fibre appearance and feel. It was developed in the early 1930s by R. H. Kägi for Heberlein AG in Switzerland (then patented as "Helanca") first in a discontinuous process and, almost at the same time, in a continuous process by D. Finlayson and F. Happey of British Celanese, Ltd. in Great Britain and for the Celanese Corporation of America in the United States. [14,15] Nowadays, it is a continuous process that utilises the thermoplastic properties of yarn. As shown in **Figure 3**, the passing yarn is [12,16]:

1. stretched ("drawn") to increase molecular orientation and crystallinity,
2. highly twisted to deform each filament,
3. heated to break intermolecular secondary bonds,
4. cooled to fix the twisted shape by re-forming secondary bonds,
5. untwisted, post-treated, and wound.

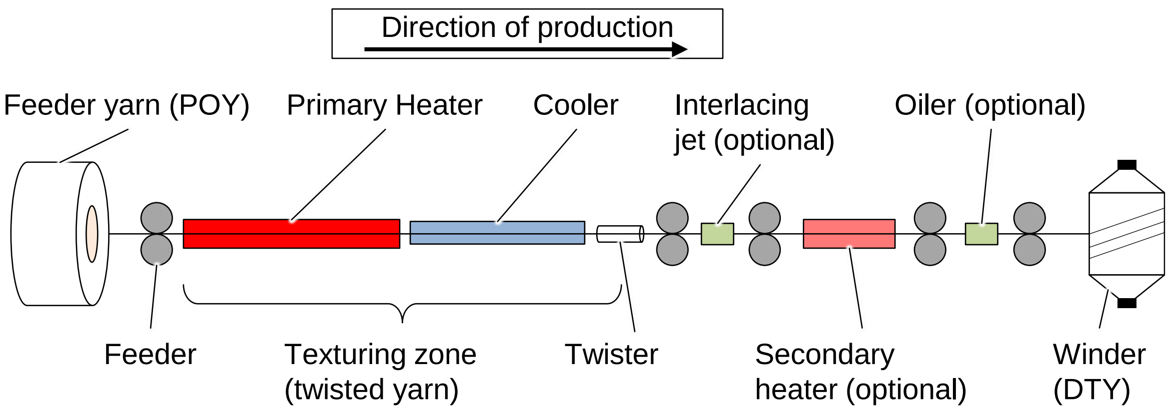

Figure 3: Schematic of the false-twist texturing process. Created by the authors based on [2,3,5,12,17,18]

The heaters in FTT are characterised by their substantial length and inefficiency (typically 2-2.5 m, with 85-90 % of energy lost as waste heat), accounting for 40-50 % of a texturing machine's total energy consumption [8,19]. Consequently, reducing the energy requirements of these heaters significantly lowers the overall energy footprint. Furthermore, reducing heater length shortens the texturing zone, increasing process speed and productivity, as the texturing zone length is one factor influencing process speed. It is limited by process instabilities, specifically periodic variations in yarn tension known as (tension) surging, which results in negative DTY properties. A shorter heater length automatically raises the surging speed, the threshold production speed at which these instabilities occur, allowing for higher operating speeds and, therefore, increased productivity. The everlasting long-term goal of combining POY and DTY production in a true single-step process requires DTY production speeds to exceed 5000 m/min – even higher than typical POY production speeds, as another drawing step takes place in texturing with a factor of about 1.7. In the last decades, production speed has increased by four or five times – however, surging usually occurs slightly above 1000 m/min, and a combined POY-DTY process is still not possible. [7,12,16,18,20] However, to ensure consistent DTY quality, the thermal energy transferred to the yarn must remain constant; thus, the temperature of shortened heaters must be increased. This temperature elevation is subject to upper limits, is inherently inefficient, and may result in thermal damage to the yarn. [8,12].

A compact, alternative, and more efficient solution for heat input in FTT could lower DTY production costs while maintaining the desired yarn feel. Moreover, such a solution would reduce the need for imported primary energy, leading to further cost savings and contributing to the Federal German Climate Protection Plan 2050 and the Federal German Strategy for Adaptation to Climate Change, as set out in the Federal Climate Adaptation Act [21–23]. Furthermore, this contribution supports the United Nations' 17 Sustainable Development Goals, with a focus on Climate Action and Sustainable Cities and Communities [24]. The derived goals for the research are therefore:

- A reduction of the energy consumption of the FTT heater by at least 40 %, as well as
- an increase in productivity via a 20 % increase in production speed.

The innovative approach (**Figure 4**) to achieving these goals is to develop a short (< 0.8 m) and energy-efficient microwave heater suitable for high production speeds and the corresponding polymeric yarn materials. This heater will shorten the texturing zone, allowing for higher production speeds without tension surging. Furthermore, microwave radiation penetrates the material more deeply than convection heating, which only heats the surface and then transfers heat to the yarn's interior. Current short high-temperature electric heaters

(HTI) with a length of 1 m create a strong heat gradient in the yarns, resulting in temperature differences between the outside and the core of the yarn and leading to a different yarn feel. As PET, the main polymer used for man-made fibre production, can be heated via microwave radiation due to its molecular structure, a microwave heater poses a feasible approach. [1,25] So far, microwave heating has not been utilised in FTT. Current uses in textile technology include carbon fibre production and composite curing, as well as the drying, dyeing, printing, or finishing of textiles and yarns. [26–30]

Certain challenges arise when using microwaves in false-twist texturing. The consistency of applied heat is a highly important quality criterion in FTT, as deviations along the yarn axis or from position to position render the yarns unusable in downstream processes due to streaks and other defects arising from variations in polymer crystallisation. [12,18,20,31,32] Adding to that, the yarn travels with high speeds through the texturing machine and, thus, also through the heater. Yarn speeds usually range from 500 m/min at the beginning of the process, when POY is fed into the machine, to 1000 m/min (17 m/s) at the winder, due to the desired drawing of the yarn. The yarn speed in the heater where the microwave will be applied lies between those values. On top of that, the yarn is twisted up to 3000 times per meter, resulting in up to 60000 twists per second. These movements introduce vibrations into the yarn, posing challenges for the process, especially the required constant temperature, which strongly influences the resulting yarn properties. These are crucial for downstream processes like knitting. Another critical factor is the diameter of the yarns susceptible to texturing. Typical yarn diameters range from 100 to 125 µm (about 83 to 167 dtex final titre in the DTY). The input yarn (POY) is thicker, of course, as the yarn is drawn during texturing to align the molecules – ranging from 140 to 290 dtex on average. [12,33] Current textured yarn production even trends towards even finer yarns in the range of 20-50 dtex. Therefore, a deep penetration depth is not required, which facilitates the usage of 5.8 GHz and smaller microwave resonant cavities in the process. Nonetheless, precise focus on the intended electromagnetic field is needed to guide the energy into the yarn for heat generation. [34,35] Adding to that is the effect of heater contamination, caused by debris containing polymer, polymer additives and spin finish. Long-term contamination must be evaluated, and either sophisticated cleaning cycles or a self-cleaning mechanism needs to be introduced. [12]

Furthermore, the dominant yarn material in FTT, PET, has a weak polarity, especially below its glass transition temperature, where molecules are rigid and bonded by strong covalent forces. Therefore, a strong electromagnetic field is needed (at least 1 MV/m, based on the given process parameters) to generate sufficient heat in the material, usually achieved by increasing the power input or by more effectively leveraging the electromagnetic field distribution and amplification in the resonator. Once the yarn is heated by sufficient electromagnetic energy, the molecules become more mobile above the polymer’s glass transition temperature, thereby facilitating a greater temperature increase in the material. This effect can lead to a so-called thermal runaway if not properly controlled, which, in the worst case, can result in yarn breakage and machine downtime. [36] Therefore, to monitor heat application during texturing with the challenges outlined above and to validate the novel heater’s functionality, a cost-effective temperature sensor with suitable lens optics for thin, fast, and spinning polymeric yarns is being developed and validated at lab and pilot scales, as current solutions for yarn temperature monitoring are not sufficient. This sensor, however, is not part of this work but will be published in upcoming work.

All in all, microwave heating offers great potential for yarn texturing facilities. In Germany, a yarn texturing company could save 961 to 25950 MWh annually, i.e., 343 to 9264 t CO_2 equivalents per year. In China, where the main textile industry is located, those CO_2 equivalents can reach even higher values due to a higher emission index, resulting in approx. 558 to 15051 t CO_2 equivalents per year. Therefore, the MicroHeatTex project and this work directly influence the achievement of climate goals. Those numbers are proportional to the number of texturing machines sold to customers using the novel and efficient microwave heating technique. With an annual sale of 2400 texturing machines and a market penetration of 5 %, between 5768 and 31140 MWh of energy can be saved annually worldwide, which, with a global emissions index of 466 gCO_2/kWh, results in annual CO_2 savings of between 2688 and 14511 tonnes. [37]

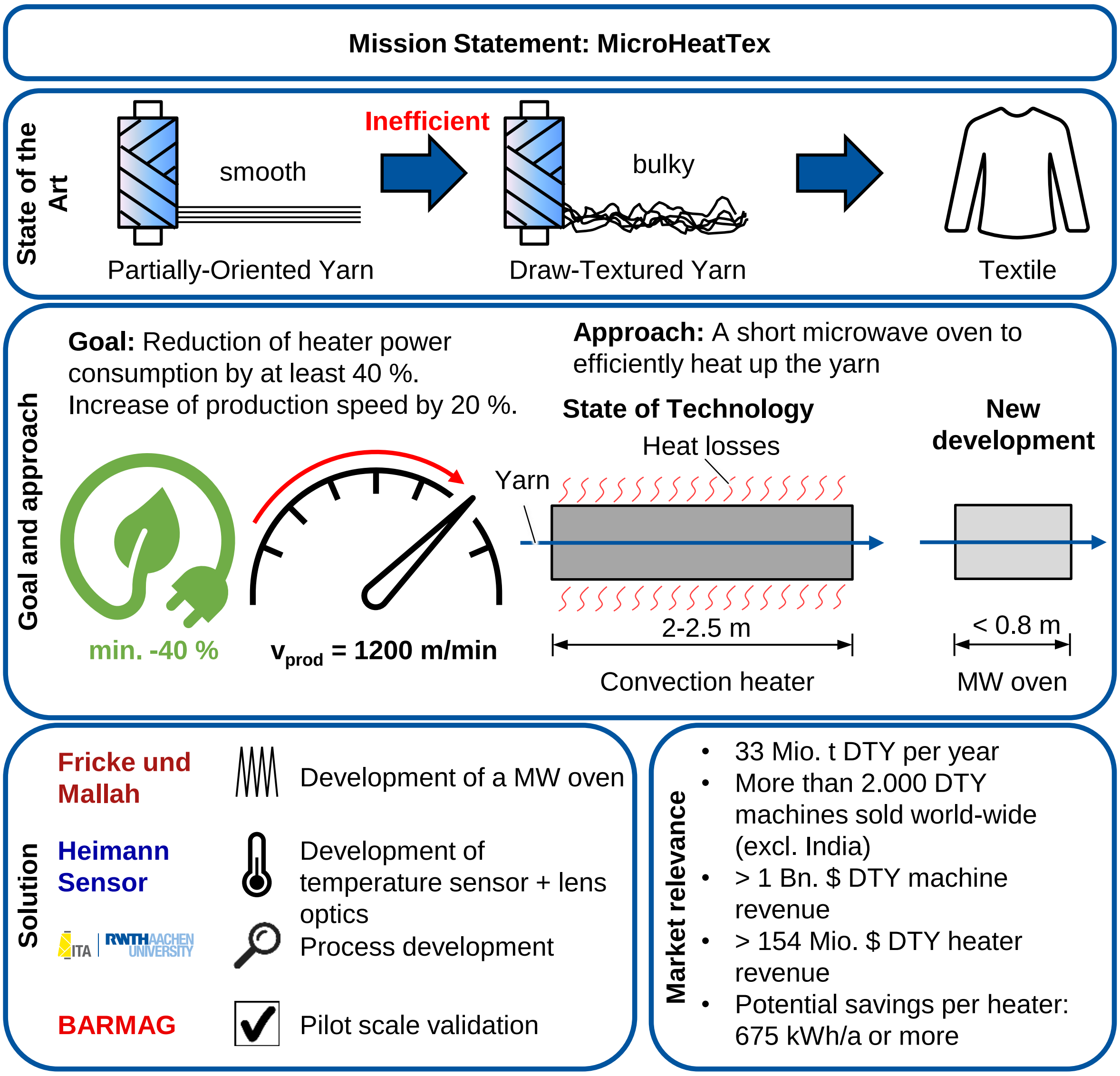

Figure 4: Mission Statement of the project *MicroHeatTex*

2. Fundamentals of Microwave Heating

2.1 The Theory of Microwave Heating

Electromagnetic waves are transverse waves composed of coupled oscillating electric fields $\vec{E}$ and magnetic fields $\vec{H}$, which propagate through vacuum or material media. The behaviour of electromagnetic waves is described by Maxwell's equations, which unify the phenomena of electricity and magnetism. Microwaves are harmonic solutions of Maxwell's equations in the range of 300 MHz to 300 GHz. To uniquely determine the electromagnetic field in a given physical system, boundary conditions must be specified; this is the underlying principle used by simulation software to compute the electric field distribution. [25,38–40]

In the false-twist texturing process, polymeric yarn materials that require heating, such as PET and polyamide, are Class II materials (inorganic solids, organic solid crystals, and liquid crystals). For these materials, microwaves interact primarily with the electric dipoles or polarisable groups within the molecular structure. Free rotational motion is restricted in these solids. Both the orientation polarisation of polar groups and the excitation of local vibrations of atoms or molecular segments cause heating. Lattice flaws or vacancies can also function as effective dipoles in polar solids or ionic crystals. When ions move between sites in response to a microwave electric field, their dipole orientations shift, thereby producing heat. These units become mobile as the temperature rises, which improves polarisation and microwave energy absorption. [41]

To quantify the microwave energy absorbed by the corresponding material, the volumetric power density P can be expressed as a function of the electric and magnetic fields as well as the material properties [35,41]

$$P = \frac{1}{2}\left(\varepsilon''\omega|E|^2 + \mu''\omega|H|^2 + \sigma|E|^2\right) \tag{1}$$

- where $\omega = 2\pi f$ is the angular frequency,
- f is the frequency,
- ε'' and μ'' are the imaginary parts of permittivity and magnetic permeability,
- and σ is the electrical conductivity.

For nonmagnetic, poorly conducting materials like PET, both the magnetic-field contribution $\mu''\omega|H|^2$ and the conduction term $\sigma|E|^2$ are negligible. Instead, heating occurs primarily because the microwave's oscillating electric field interacts with internal electric dipoles and polarizable groups. Thus, the absorbed power is dominated by the electric field effects. Instead of applying accurate material models to map molecular relaxation effects, such as the Havriliak-Negami model with mathematical correction factors, the Debye relaxation model is used here to approximate the material behaviour. Therefore, an additional term accounting for the conduction loss can be neglected when heating non-conductive chemical fibre materials. Once the microwave field strength, frequency, and complex dielectric constant of the material are determined, the average absorbed power of the material can then be calculated as [34,35,42,43]

$$P = \frac{\varepsilon_0(\varepsilon'_s - \varepsilon'_\infty)\omega^2\tau}{1 + \omega^2\tau^2}|E|^2 \tag{2}$$

- where $\varepsilon_0 \approx 8.854\times10^{-12}\ \mathrm{F\cdot m^{-1}}$ is the permittivity of free space,
- ε'_s is the static permittivity,
- ε'_∞ is the high-frequency permittivity,
- and τ is the relaxation time of the molecular dipoles.

This theoretical derivation proves that the absorbed power density P is directly proportional to the square of the electric field magnitude $|E|^2$:

$$P \propto |E|^2 \tag{3}$$

Unlike traditional convective or radiant heating, microwave heating generates heat directly within the material itself. An essential factor in heating performance is the penetration depth, defined as the distance from the material's surface at which the incident microwave power drops to $\frac{1}{e}$, approximately 37 % of its original value. [34,44] Industrial microwave processing is generally performed at frequencies reserved for industrial, scientific, and medical use (ISM frequencies), namely 915 MHz, 2.45 GHz, 5.8 GHz, and 24.124 GHz. Among these, microwaves operating at 2.45 GHz are most commonly used. The primary reason is that 915 MHz magnetron devices are physically too large, while 5.8 GHz microwaves have a very shallow penetration depth D_p, which is inversely related to the frequency f: [34,35]

$$D_p \propto \frac{1}{f}. \tag{4}$$

However, the limited penetration depth of higher-frequency microwaves is not a drawback for false-twist texturing. Since the yarns and filaments have small diameters (typically only a few hundred micrometres), effective internal heating is easily achieved. Operating at 5.8 GHz offers two distinct advantages: the penetration depth perfectly matches the micrometre-scale filaments, and the shorter wavelength allows for a more compact resonant cavity with highly localised heating zones. This space-saving design facilitates easy integration into the processing machine. Therefore, the cavity geometry analysed in this study focuses on a 5.8 GHz operating frequency.

2.2 The Structure of a Microwave Oven

A full microwave heating apparatus typically includes several components that work together to generate, guide, and trap electromagnetic energy within a specific region. As illustrated below, the main elements involve a microwave generator, a tuner, a waveguide, and the resonant cavity (**Figure 5**). [45]

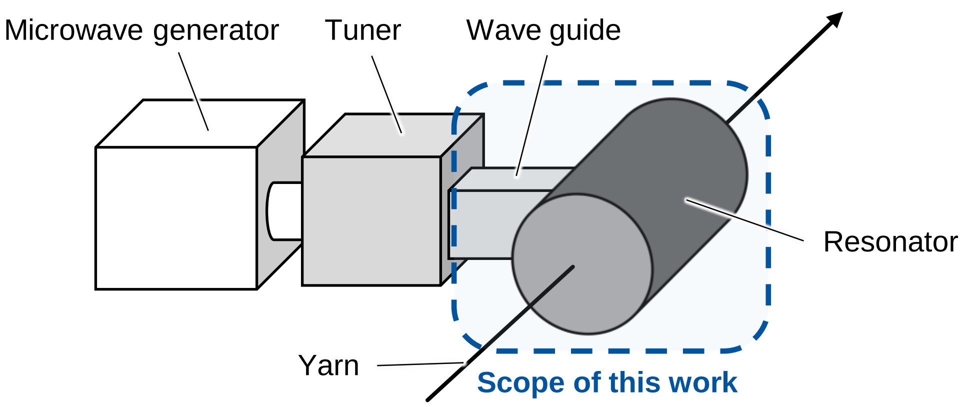

Figure 5: Schematic of a microwave heating apparatus with a yarn passing through

A microwave generator, such as a magnetron or a semiconductor-based microwave generator, produces electromagnetic waves at the designed ISM frequencies. The total energy available for further excitation of the resonant cavity is determined by the generator's output power and frequency stability. The generated microwave passes through a matching network, or tuner, which can be adjusted to achieve impedance matching between the source and the downstream waveguide-cavity system. Proper adjustment of the tuner reduces reflected power to the generator, thereby improving the overall system performance. Next, a waveguide with a hollow metallic structure is used to transmit the energy, confining and directing the generated electromagnetic waves via boundary conditions imposed on the electric and magnetic fields. Rectangular waveguides are widely used in industrial systems because their dimensions are standardised for specific frequency bands. Although the present work does not involve designing the waveguide itself, a basic understanding of wave propagation in rectangular waveguides is required for correctly modelling how energy enters the resonant cavity. The theoretical background is discussed below. The guided microwaves eventually reach the resonant cavity, where multiple reflections at the conductive walls create standing waves. Discrete resonant modes are excited, resulting in spatially localised regions of high electric field intensity, depending on the cavity geometry and boundary conditions. As demonstrated before, the absorbed microwave power is proportional to the square of the electric field magnitude $P \propto |E|^2$, making these electric-field maxima crucial for efficient heating in the false-twist texturing process. [45]

Rectangular waveguides, the most commonly used waveguide type in industrial applications, support a set of discrete propagating modes that can be conceptually understood as the superposition of plane waves. Operating the waveguide in a single-mode regime ensures a stable, predictable field profile. The single-mode prevents higher-order modes from being excited, thereby avoiding undesired field distributions and reducing power distortion. [45] Since mode propagation depends on the relationship between the operating frequency and the waveguide's transverse dimensions, it is necessary to determine appropriate waveguide dimensions for operation at 5,8 GHz. The relationship between cutoff frequencies of different modes and the size of the rectangular waveguide is given by [25,46]

$$f_c = \frac{c_0}{2}\sqrt{(\frac{m}{a})^2 + (\frac{n}{b})^2} \quad (5)$$

where $c_0 \approx 3\times10^8$ m/s is the speed of light, a is the wider dimension of the rectangular waveguide, b is the narrower dimension, and m, n are the mode indices.

According to [47], the waveguide type “WR159” with dimension 40.386×20.193 mm is commonly used for microwaves at 5.8 GHz. The reason is that the cutoff frequency of its fundamental TE_{10} mode is approximately 3.71 GHz, which is well below the operating frequency of 5.8 GHz, ensuring low-loss propagation of the dominant mode. In contrast, the next higher-order modes, most notably TE_{20} and TE_{01}, have cutoff frequencies of approximately 7.42 GHz, placing them safely above the operating frequency of 5.8 GHz. Therefore, WR159 waveguides operate strictly in a single-mode regime at the intended frequency without interference from higher-order modes. The results of the calculation fully agree with publicly available industrial specifications [47], proving that WR159 is a wise choice for the simulation experiment.

3. Materials and Methods

To achieve the research goals, a microwave oven is first simulated using Genetic Algorithms and simulation software, in an iterative optimisation approach, to identify unconventional resonator geometries that maximise the electric field strength along the yarn path. The information generated will be used to develop the microwave oven. The hardware used for the implementation and simulation is an ASUS Gaming Laptop with the specifications given in **Table 1**.

Table 1: Adaptive meshing parameters used in Ansys HFSS

Parameter	Value
Laptop model	ASUS TUF Gaming F15
Operating System	Windows 11 23H2
CPU	Intel i7-12700H
RAM	16 GB
GPU	*Not supported by Ansys Teaching License*

The following **research hypothesis** is proposed: Using the optimisation workflow developed in this research paper, the microwave resonator geometry can be iteratively optimised using a Genetic Algorithm and high-frequency simulation software to find an unconventional geometry that leads to an electric goal field strength of more than 1 MV/m, which is sufficient to heat the PET yarn beyond 190 °C.

3.1 Genetic Algorithm for the Optimisation Problem

Complex optimisation problems require modern metaheuristic algorithms inspired by nature. A commonly used approach for single-objective optimisation problems is the bio-inspired Genetic Algorithm (GA) with differential evolution. [48] Key advantages include global search capabilities applicable to high-dimensional, multimodal, and nonlinear optimisation problems, as well as robustness and parallelism. Furthermore, a GA does not rely on gradient information and imposes few mathematical requirements on the objective function, making it applicable to real-time system modelling and black-box optimisation problems. The working principle consists of the following steps: initialisation, fitness evaluation, selection, crossover and mutation. A globally optimal solution is not guaranteed, so the parameters and strategies have to be adjusted in practice. [49–51]

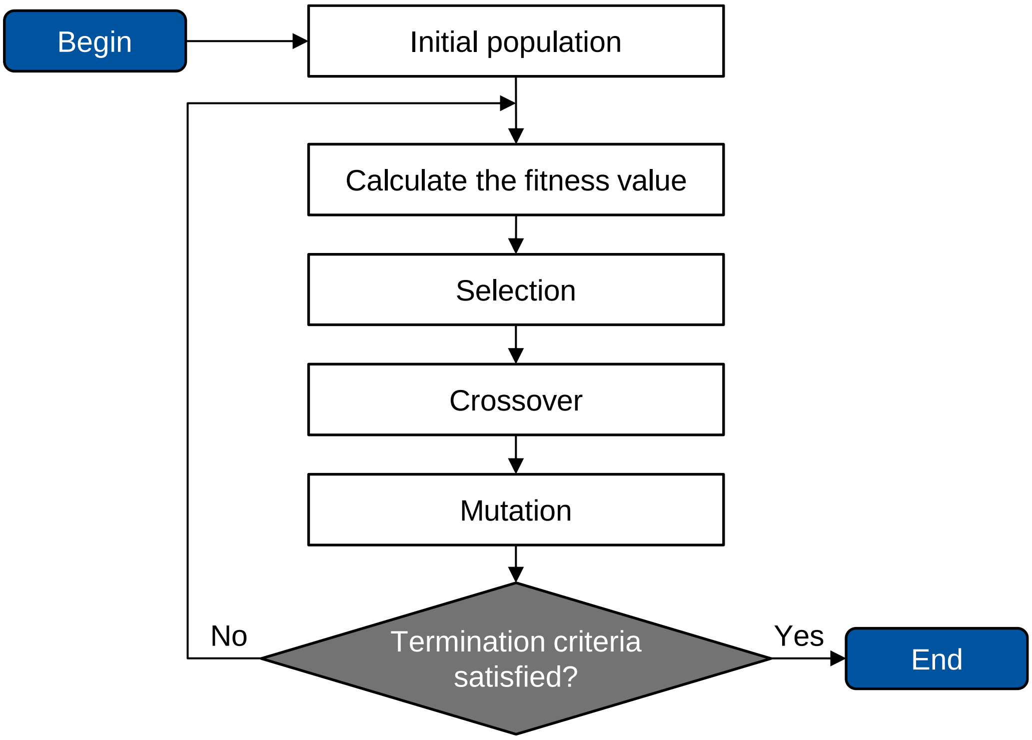

Figure 6: Flowchart of the standard genetic algorithm. Created by the authors based on [50,52]

3.2 Parametrisation of the Cavity Geometry

The resonant cavity to be optimised needs to be expressed appropriately through a mathematical parametrisation with sufficient geometric freedom. The geometry must allow the yarn to pass directly through without interruption or bending, thereby serving as the structure's primary axis. Consequently, the three-dimensional cavity geometry can be defined by specifying a two-dimensional surface and extruding it along the primary axis. In this representation, the surface determines the cavity's radial profile, while the extrusion operation ensures a straightforward channel for the filament. This abstraction reduces the three-dimensional parametrisation problem to a two-dimensional one without violating the physical constraint imposed by false-twist texturing. The predefined waveguide is then directly attached to the side of the resonant cavity, as illustrated below.

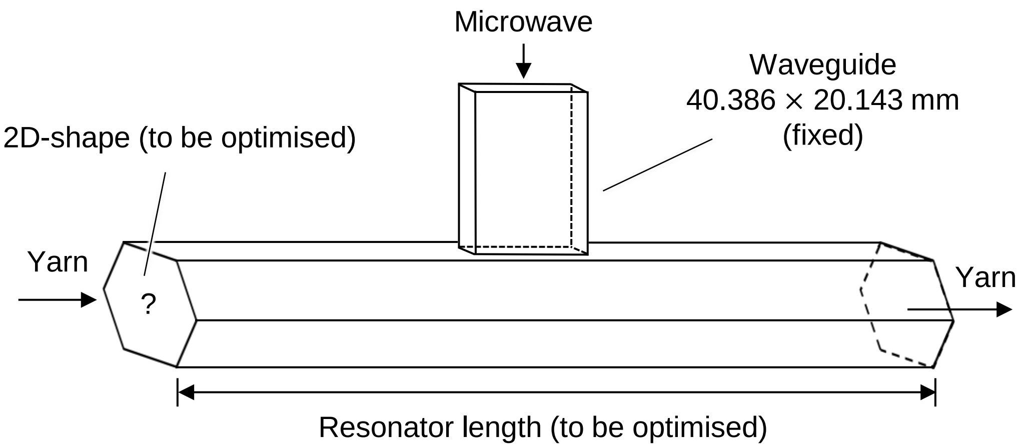

Figure 7: Extrusion-based resonant cavity parameterisation with waveguide

A “surface-contour” method is used to represent the extruded 2D surface. The method was particularly applied for the optimisation of dielectric resonant antennas. It works especially well with global optimisers. [53,54] The surface-contour method can be conceptually described by a three-step procedure. First, the height values are defined at a finite set of control points arranged on a regular grid. Next, a continuous three-dimensional surface is reconstructed from these discrete values using an interpolation technique. Finally, the target two-dimensional contour is extracted as the intersection between the interpolated surface and a plane at a constant height (cf. **Figure 8**). Through this method, a continuous planar geometry with a high degree of shape flexibility can be described using only a limited number of discrete, optimisation-friendly variables. Furthermore, the control point values can be naturally expressed in matrix form, allowing for an efficient exploitation of symmetric geometries.

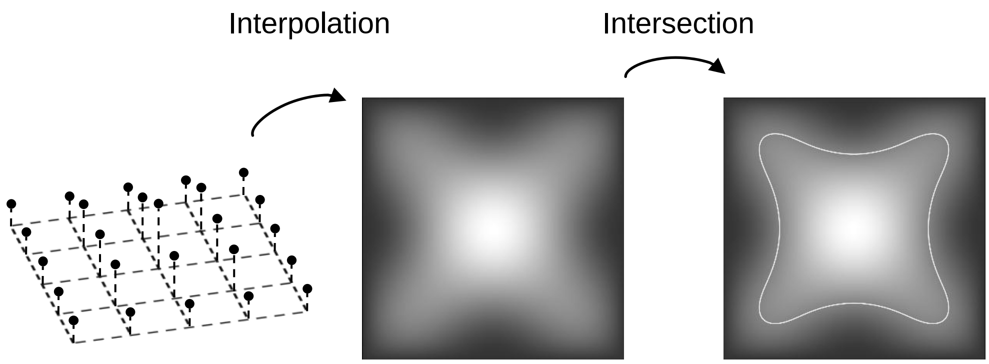

Figure 8: An example of conceptual steps of the surface contour method

From this parametrisation, a 3D model is generated in a decoupled software module which can be used for subsequent simulations. The model generation pipeline is implemented in Python 3.10.19 (Python Software Foundation, Beaverton, OR, USA) with support from the libraries CadQuery 2.3.1, SciPy 1.15.3, and Matplotlib 3.10.6. [55,56]. The pipeline chooses a valid (closed) contour and interpolates a smooth 2D profile from it. This profile is extruded along the yarn axis, with cylinders representing the yarn entrance and exit added. The final result is saved as a .step file. The microwave port is added, and faces are defined so the simulation setup can automatically locate and assign boundary conditions to the relevant faces.

3.3 Optimisation Workflow with Simulation in ANSYS HFSS

The fitness value determination used in the Genetic Algorithm is realised via high-frequency electromagnetic simulations with excitation powers of 60 and 100 W, respectively. To succeed, **simplifications and assumptions** are made to simulate the 3D resonator geometry and its corresponding electromagnetic field. The simulation relies on numerical computation of Maxwell’s equations, with only limited realistic physical behaviour, to preserve the dominant effects governing the electromagnetic field distribution. This approach saves computational costs and often increases the model stability. The simulation is performed in the frequency domain, assuming steady-state electromagnetic field distributions. The metallic parts of the resonator are modelled using a finite-conductivity boundary rather than volumetric bodies with explicit thickness, representing the walls via an impedance formulation. The surface roughness, microscale defects, and material inhomogeneities are not considered. Electromagnetic-thermal coupling is not regarded in this work. Only the electromagnetic field distribution is calculated during simulation, and no temperature information is generated. Therefore, the electrical conductivity is assumed constant and independent of temperature. Material parameters are assumed to be frequency-independent over the operating band, which is reasonable since the simulation is conducted at a single frequency, 5.8 GHz. The yarn is not explicitly modelled, as it is electrically small, and thus only small perturbations are assumed from it, compared to the operating wavelength of 51.7 mm at 5.8 GHz. Omitting it avoids unnecessary mesh refinement, improving the simulation efficiency.

The simulation is performed using **Ansys HFSS™** (ANSYS, Inc., Canonsburg, PA, USA) with the Finite Element Method (FEM) using the Teaching License provided by RWTH Aachen University, Aachen, Germany. [57] Using this license, only single-thread (serial) simulations are possible. The Driven Modal Solver is used in this work. With it, the electromagnetic response under a defined source excitation and operating frequency can be determined – in contrast to the Eigenmode Solver, which only calculates the natural resonant frequencies and corresponding field distributions based on the geometry and material properties. Adaptive Meshing is applied with the parameters given in **Table 2**. With these parameters, some precision might be lost at corners and edges. Still, the computation time remains acceptable (in the order of a few minutes in most of the cases simulated in this work). Furthermore, the field distribution along the yarn path through the resonator's centre is accurately simulated.

Table 2: Adaptive meshing parameters used in Ansys HFSS

Parameter Name	Value	Description
BasisOrder	1	First-order basis functions for field approximation
DoLambdaRefine	True	Mesh refinement based on the wavelength
DoMaterialLambda	True	Mesh refinement according to material properties
LambdaTargetForIESolver	0.15	Target max. element size relative to wave length
Target	0.1	Overall mesh accuracy target
MaximumPasses	10	Maximum number of adaptive mesh passes
MinumumPasses	3	Minimum number of adaptive mesh passes
PercentRefinement	30	Max. percentage of elements refined per pass

In Ansys HFSS, the electromagnetic field information can be **extracted** at specified 3D coordinates. A discrete set of electromagnetic field magnitudes along the yarn path can be obtained as a file for further processing. As the absorbed electromagnetic power is proportional to the square of the electric field, a larger field magnitude results in a disproportionately stronger heating effect. To rapidly raise the yarn temperature while minimising heat dissipation to the surrounding environment, the maximum field strength is chosen as the primary performance indicator, with higher values indicating better heating performance.

Coupling of Python scripts and Ansys HFSS is achieved using PyAEDT – the official Python interface by ANSYS. The operating system's file system manages the interconnections among different software tools. All results are always stored on disk for risk minimisation, reproducibility, and subsequent data analysis.

The optimisation using the Genetic Algorithm first initialises with random individuals via the surface-contour method, which are then filtered with multi-thread acceleration to ensure suitable geometries. The simulation results are ranked by the maximum field strength along the yarn path within the resonator cavity. Selection strategies that rely solely on absolute values, however, may lead to excessive selection pressure and early convergence, potentially trapping the algorithm in a local maximum. Therefore, in this work, individuals are ranked by their relative performance, and the most suitable parents are chosen. Furthermore, elite individuals are identified and permanently recorded until a better one is found, to ensure that the best-performing individuals are not abandoned.

Once the parents have been identified, they are combined to generate children for the next generation. The design variables are the control point values for the surface-contour method, which is highly abstract. They lack geometric meaning, so arbitrary mixing of points will yield meaningless shapes. Therefore, a single-point crossover strategy is employed (see **Figure 9**). After crossover, each child has a probability of mutating with random noise applied to each control point, preserving the overall spatial structure of the geometry while still allowing the algorithm to explore new regions of the design space.

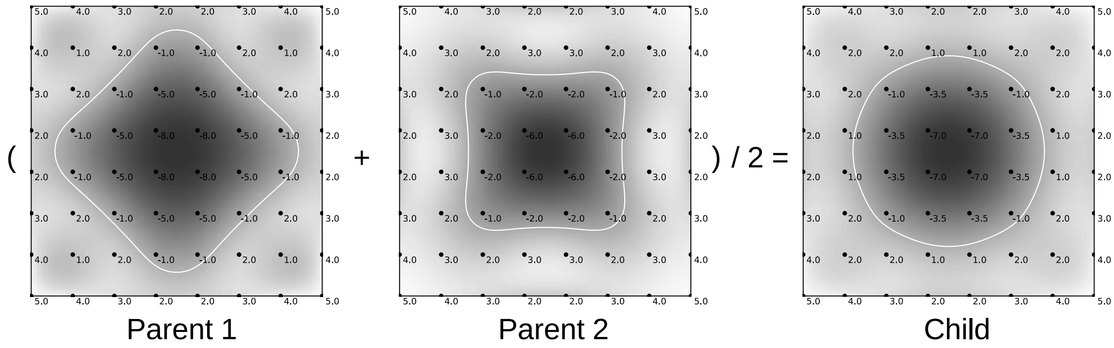

Figure 9: An example of the effect of the single-point crossover strategy

During the optimisation workflow, the population size is varied from 120 to 1000, with an initial control point value bound set between to [-100, 100]. The mutation rate is set to 0.5, with a mutation range of 20. The top 30 individuals are selected as candidate parents for the next generation. Various symmetry options are chosen to reduce computational costs.

4. Results and Discussion

The results of the iterative microwave resonator optimisation and the very first application of the temperature sensor are presented below. All simulations were conducted under the same modelling assumptions and simplifications introduced before.

To investigate the effect of different ranking probability distributions, a linear and an exponential approach are applied under otherwise identical settings. No symmetry is applied; the excitation power is set to 60 W, and the population size is set to 220. The results are shown in **Figure 10** below.

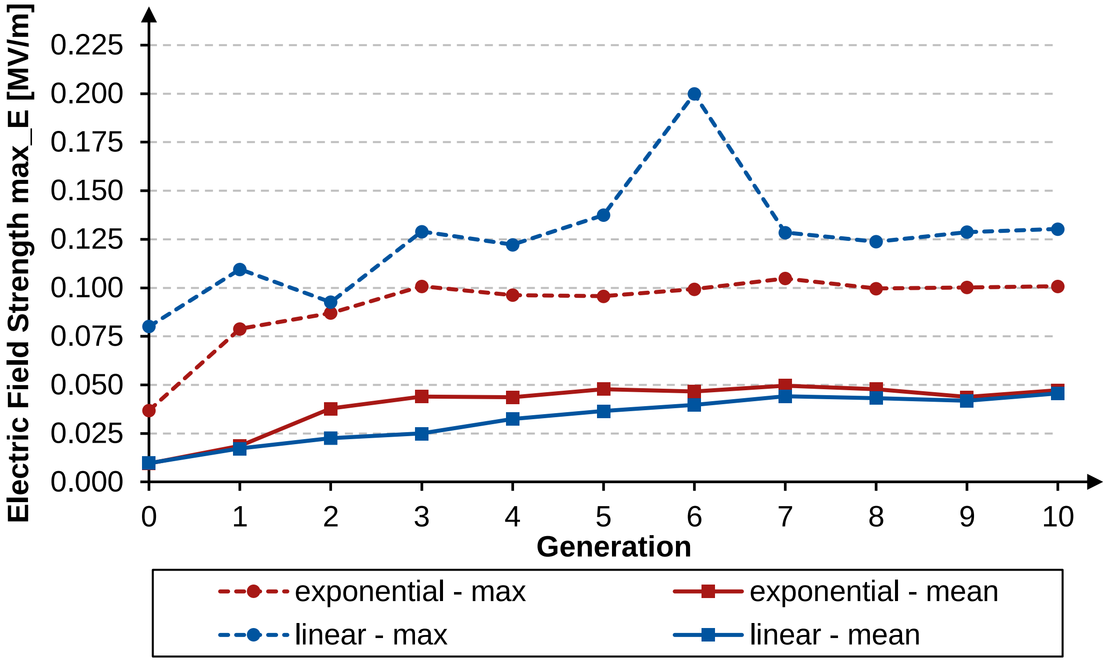

Figure 10: Evolution of simulated electric field strength using linear and exponential ranking selection probability distributions with axisymmetric shape; The excitation power is set at 60 W

It can be observed that both the maximum and the mean electric field strength increase rapidly during the early generations when using the exponential probability distribution strategy, but remain at relatively low, stable levels in later generations. This indicates stronger exploitation of the currently best-performing solutions, thereby accelerating convergence. However, this also implies that the algorithm is trapped in a local maximum. In contrast, the linear approach leads to slower improvement in the mean electric field strength, with consistently lower values until the very end, and a less stable evolution of the maximum value. It can be noticed that a markedly higher-performing individual emerges around the sixth generation (200000 V/m), which is considered to be enabled by the wider range of selection. This behaviour shows that the linear distribution explores the design space more effectively over a longer optimisation horizon, which is preferred in this work to achieve strong electric field peaks. Simulating the best resonator geometry from the above results with an increased excitation power of 100 W and the corresponding resonator length of 176.7 mm results in a max. field strength of 258084 V/m (**Figure 11**).

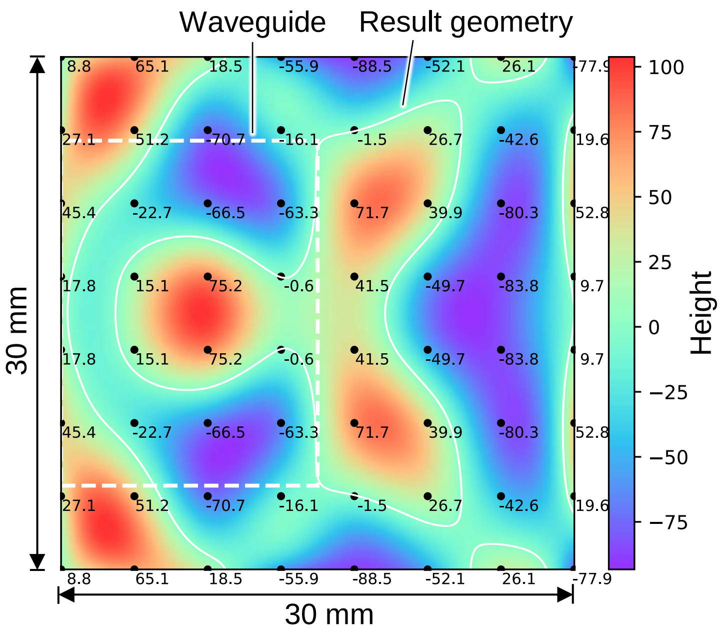

Figure 11: Electric field strength distribution at 100 W using an axisymmetric geometry with a resonator length of 176.7 mm, achieving 258084 V/m

The density of control points directly determines the dimensionality of the design space, with higher density leading to a more detailed description of the resonator cavity on the one hand, but also to higher computational costs on the other. To investigate the effect of control point density, a 6x6 grid with a population size of 250 is compared with an 8x8 grid with a population size of 500. Both cases are simulated with 60 W of excitation power, no symmetry applied, and with the same linear ranking strategy and mutation settings (**Figure 12**).

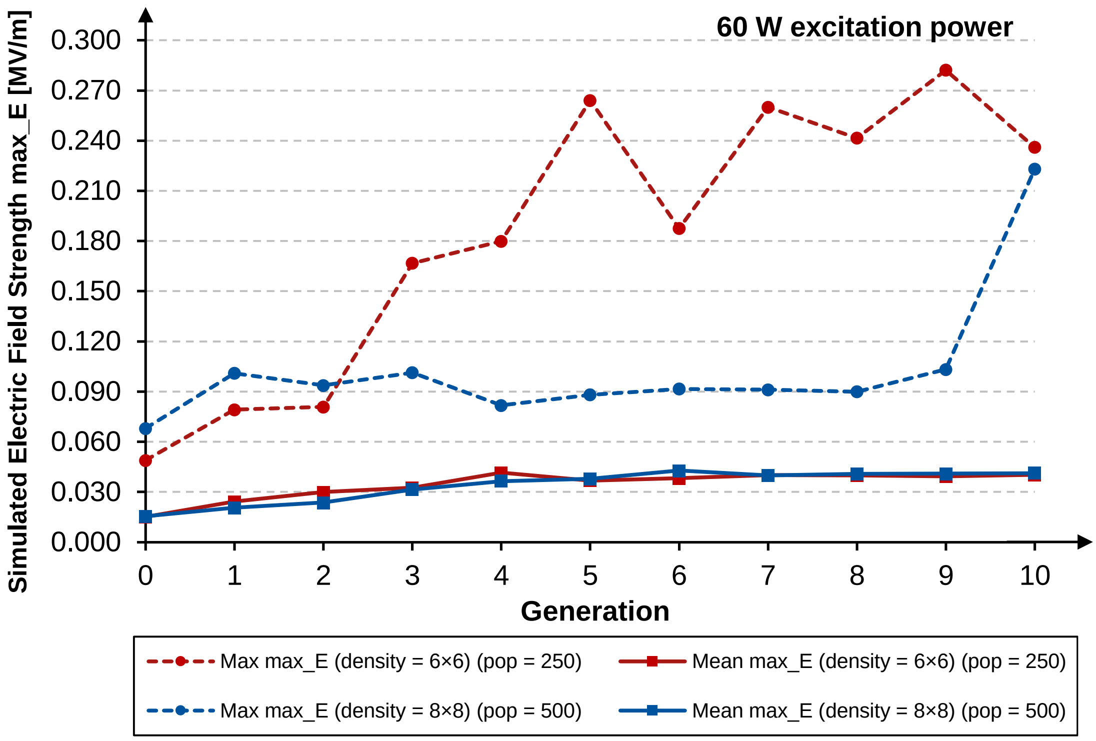

Figure 12: Evolution of the simulated electric field strength comparing a control points density of 6x6 (population size 250) to 8x8 (population size 500) with 60 W of excitation power

It can be observed that the mean electric field strength of the two cases is comparable, slowly rising in the beginning and plateauing towards the final generations. The max. field strength, however, is higher for the 6x6 case beginning with the 3rd generation. It is only in the very last generation that the 8x8 case nearly catches up with the simpler 6x6 case. In total, the 6x6 shows higher peak electric field strengths, up to 225000 V/m – the 8x8 simulation stays at a lower max. Random initialisation values could explain the field strength values at the beginning and warrant further investigation. Nonetheless, higher resolution requires a larger population size and thus a longer optimisation time to achieve comparable results. Therefore, the best individual from the 6x6 grid trial run is simulated again with 100 W and achieves 364341 V/m at a resonator length of 99.4 mm (**Figure 13**).

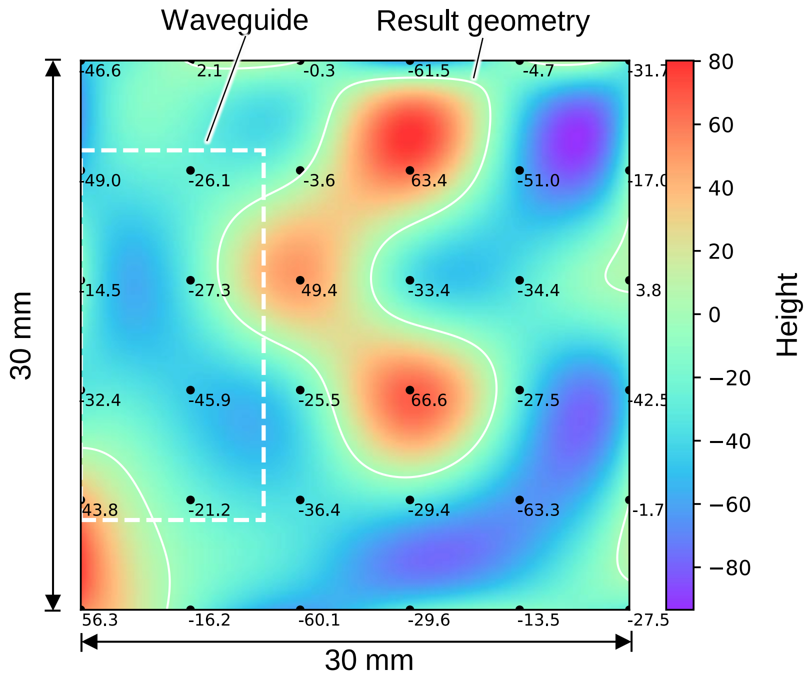

Figure 13: Electric field strength distribution of a non-symmetric resonator geometry with a 6x6 grid, a resonator length of 99.4 mm, 100 W excitation power and a max. field strength of 364341 V/m

In addition to the parameter variations given above, symmetric geometries are investigated using representative examples to speed up the optimisation process. First, a 4-fold symmetry is applied to the resonator geometry using a 4x4 control grid, a population size of 120 and an excitation power of 60 W (**Figure 14**).

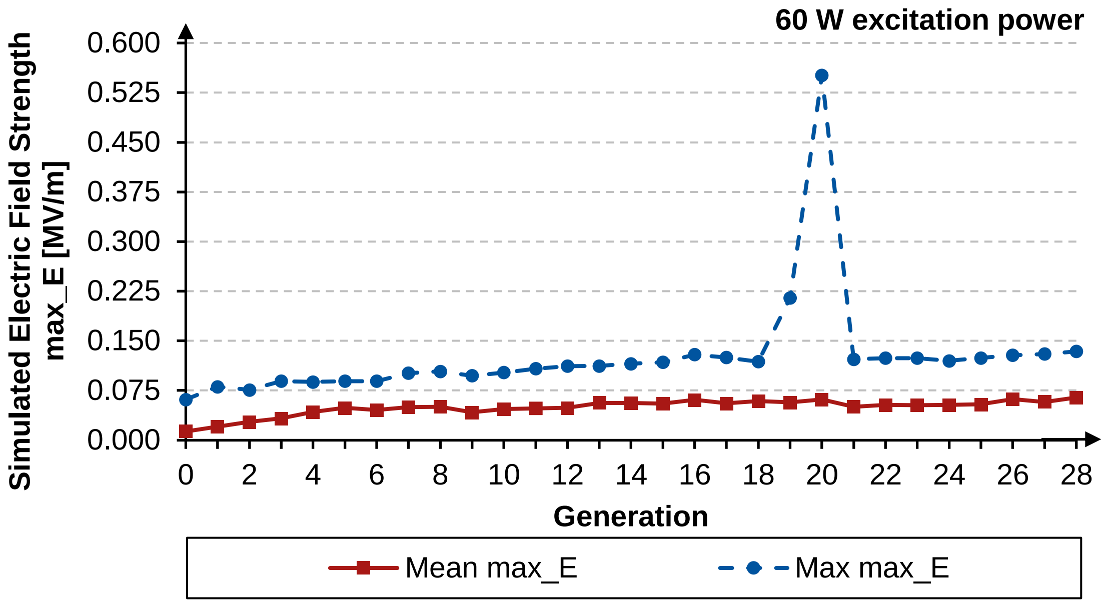

Figure 14: Evolution of the simulated electric field strength for a 4-fold symmetric shape with a 4×4 control-point grid and a population size of 120 with an excitation power of 60 W

The electric field strength steadily increases from one generation to the next, achieving a breakthrough at the 20th generation with a peak value of approx. 550000 V/m. This best individual is simulated again using 100 W, resulting in an increased max. electric field strength value of 711674 V/m. However, this value was achieved before full numerical convergence to save computational costs. Forcing full convergence still yields a peak value of 628513 V/m along the yarn path under 100 W excitation power at a resonator length of 185.3 mm, as shown in **Figure 15**, alongside the corresponding 3D geometry with 4-fold symmetry. This implies that the higher value originally obtained was an overestimation due to incomplete convergence. The peak field strength values up to 0.96 MV/m in the figure occur at the boundary regions and interfaces of the geometry, so they do not affect heat transfer into the yarn. Nonetheless, this approach seems promising, with further tweaking in the future.

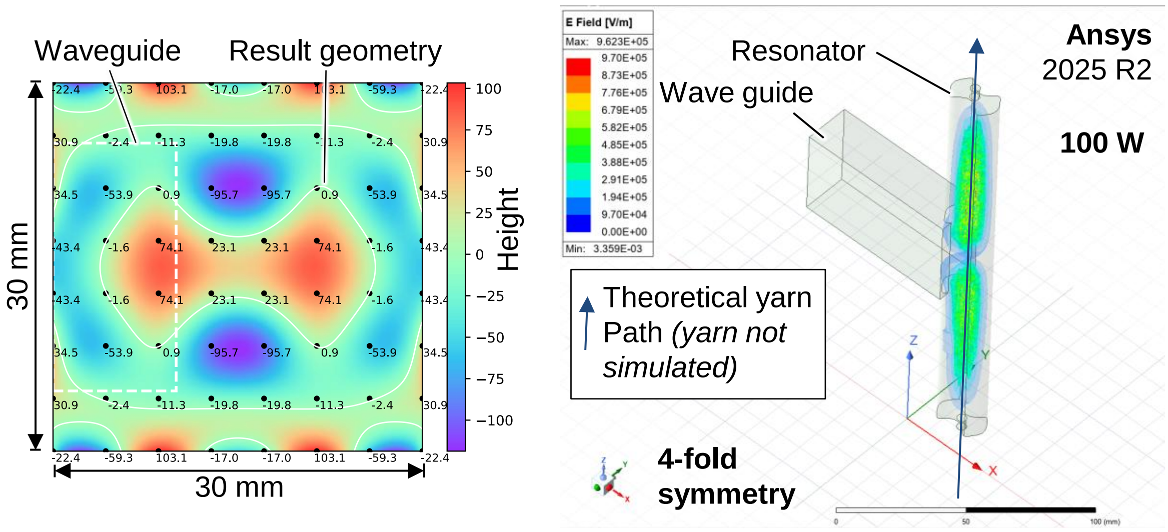

Figure 15: Left: Electric field strength distribution of a 4-fold symmetric resonator geometry with a 4x4 grid, a resonator length of 185.3 mm, 100 W excitation power and a max. field strength of 628513 V/m. **Right:** 3D resonator geometry (4-fold symmetry) with waveguide and electric field distribution at 100 W.

The evolutionary development of the resonator geometry applying 4-fold symmetry is shown in **Figure 16**. There, it is evident that different shapes are explored and evaluated, ultimately leading to the rounded double-diamond shape, which exhibits the highest electric field strength.

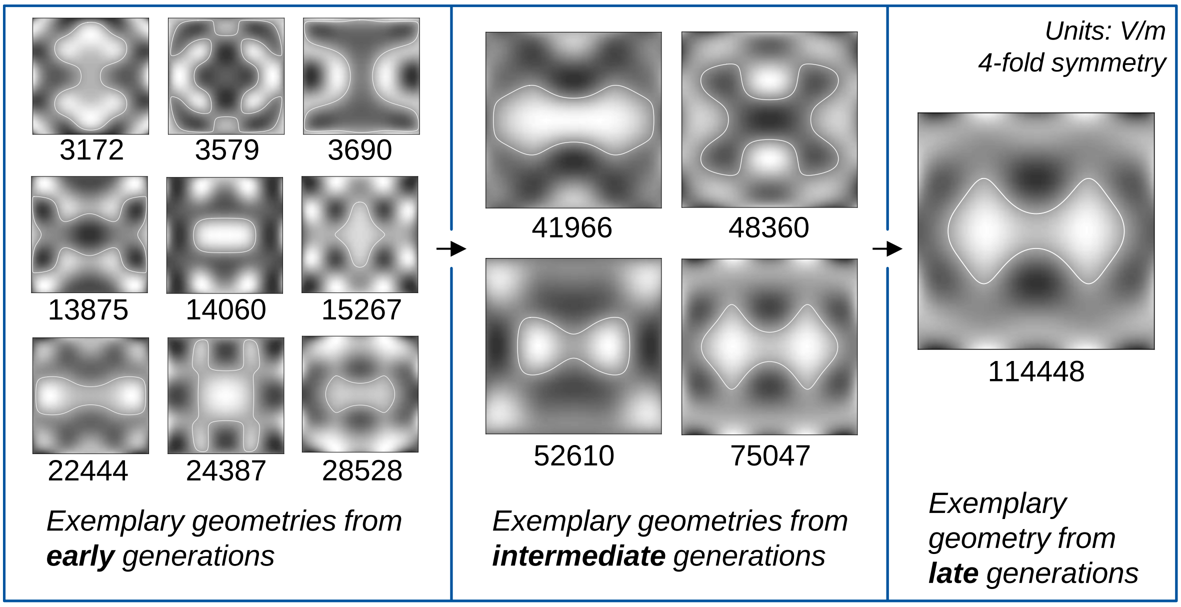

Figure 16: Exemplary evolution of 4-fold symmetric resonator geometries

Last but not least, a more complex, larger-scale attempt is undertaken, as a non-symmetric geometry combined with denser control points may yield better results – at the cost of substantial computational resources and time. Firstly, this is due to the inevitable need to assess each candidate geometry using costly electromagnetic simulations. Secondly, the optimisation algorithm needs to explore an exponentially increasing number of possibilities when the design space expands. To do so, a non-symmetric 8x8 grid is used for a resonator simulation with a population size of 1000 at 100 W (**Figure 17**).

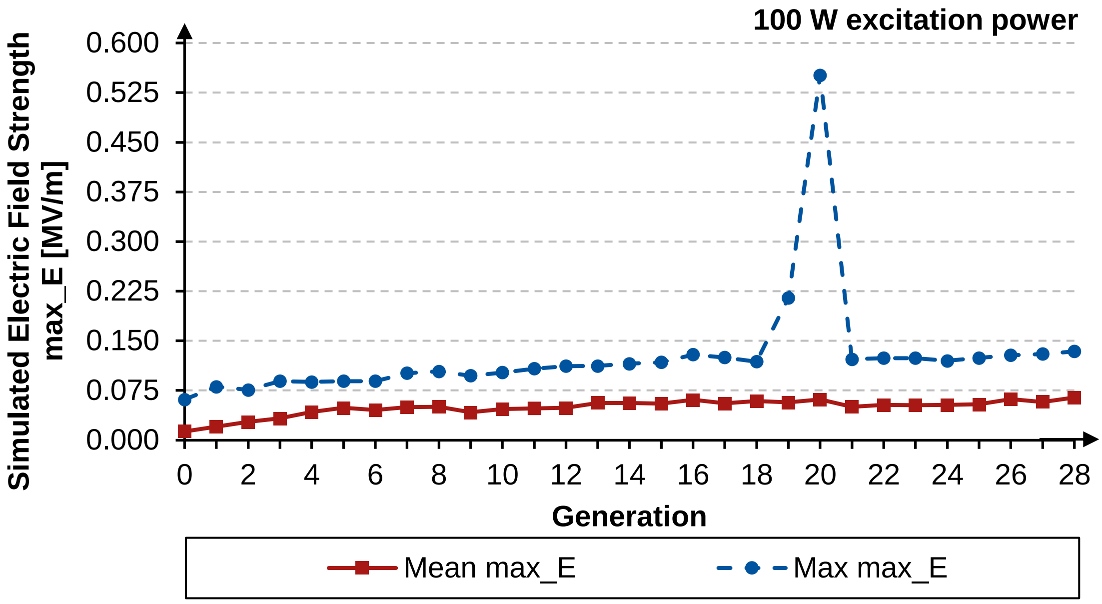

Figure 17: Evolution of the simulated electric field strength for a non-symmetric shape with an 8x8 control-point grid and a population size of 1000 with an excitation power of 100 W

During the simulation, noticeable fluctuations can be observed in the max. electric field strength with an overall upward trend. In the 36th generation, a pronounced peak is observed, reaching an exceptionally high field strength of 0.9 MV/m. Numerical instabilities in the HFSS electromagnetic solver can explain this peak. By examining the visualised electric field distribution, one can see that it appears to be an implausible anomaly (**Figure 18**).

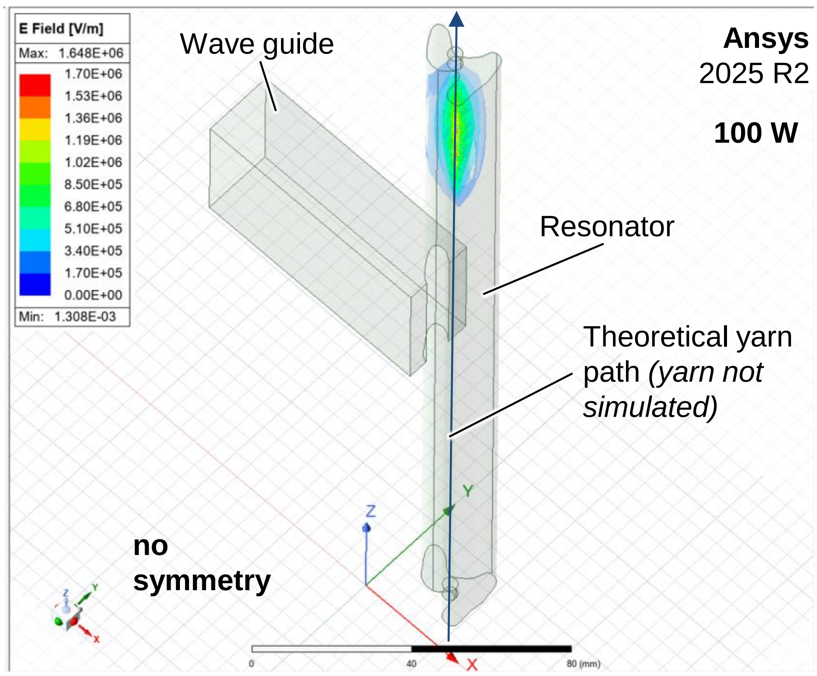

Figure 18: Electric field strength distribution of a non-symmetric resonator geometry visualised in 3D with an 8x8 grid at 100 W excitation power and an implausible field distribution with a peak of 0.9 MV/m

Subsequent simulations with higher precision removed the implausible peak in the 36th generation, yielding a lower maximum solution of 415969 V/m electrical field strength along the yarn path while maintaining numerical stability. The corresponding resonator length was 224.7 mm (**Figure 19**).

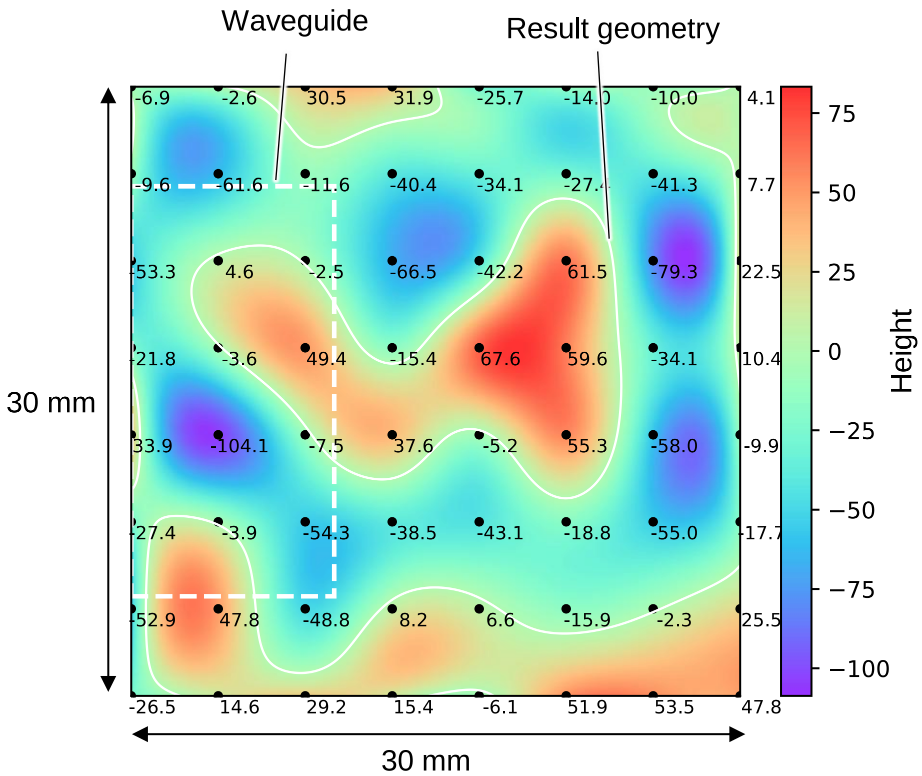

Figure 19: Electric field strength distribution of a non-symmetric resonator geometry with an 8x8 grid, a resonator length of 224.7 mm, 100 W excitation power and a max. field strength of 415969 V/m

Next, the best unconventional resonator geometry found in this work at 5.8 GHz **is compared with a conventional cylindrical resonator** at 2.45 GHz to demonstrate the potential of this optimisation process. The waveguide used in the 2.45 GHz case has dimensions of 54.61 mm × 109.22 mm, which is the standard size of WR430 [58]. Based on previous work in the field of analytical design of cylindrical microwave resonators, the resonator is set with a length of 310 mm and a radius of 46.834 mm. It is evident that under the constraints of the false-twist texturing scenario, combining the waveguide and the resonator in the manner proposed in this work does not yield satisfactory results when using a cylinder-shaped resonator. In contrast, unconventional shapes optimised by the algorithm demonstrate superior energy-concentration capabilities and achieve a more compact size. The comparison is visualised in **Figure 20**.

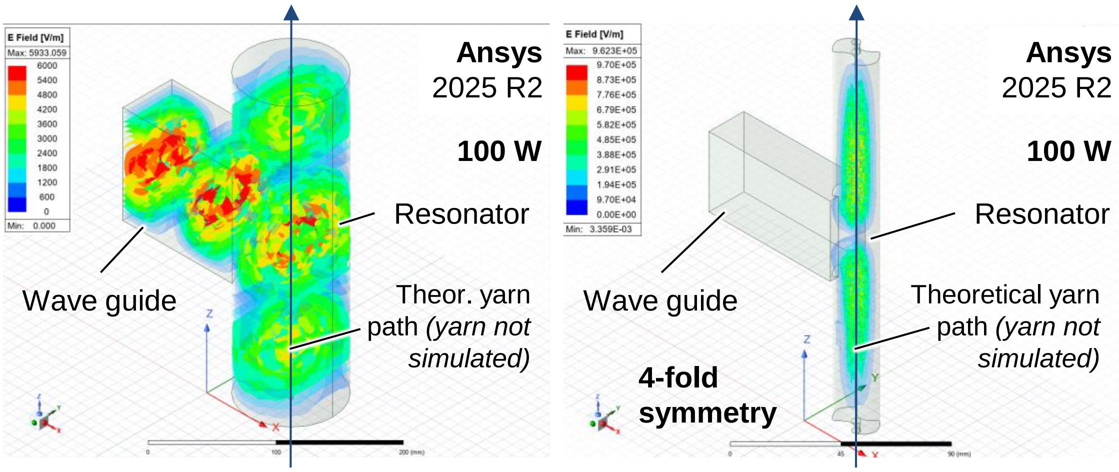

Figure 20: Simulation results of a standard cylindric resonator (left) at 2.45 GHz and the best unconventional geometry developed in this work at 5.8 GHz (right); Excitation power set at 100 W

5. Conclusion and Outlook

In this work, a novel approach to the optimisation of (unconventional) microwave resonator geometries for use as an innovative, energy-efficient heating method in false-twist texturing has been developed. The main focus was to identify geometries capable of generating high electric field strengths along the (theoretical) yarn path. To achieve this, a fully automated optimisation workflow was developed that combines geometric parameterisation, electromagnetic simulation, and an artificial intelligence-based optimisation algorithm.

A parametrisation approach based on the surface-contour method, inspired by [53], was developed to describe complex resonator cross-sections using a limited number of control-point parameters while retaining sufficient geometric flexibility. A genetic algorithm was selected to explore the high-dimensional and non-linear design space. Strategies including ranking-based selection, elite preservation, single-point crossover, and random-based mutation were combined to adapt the general genetic algorithm framework to the specific characteristics of the present optimisation problem.

The optimisation results demonstrate that using the proposed workflow, the electric field concentration can be consistently improved. Under suitable parameter settings, the algorithm reliably discovers non-intuitive cavity geometries that exhibit significantly enhanced electric field maxima. Within the investigated design space and under the applied modelling assumptions, the best-performing geometry generated a maximum electric field strength of approximately 0.63 MV/m with an excitation power of 100 W. However, despite the observed improvements, the currently identified optimal geometry cannot yet be considered a final or sufficient solution for industrial applications. The achieved electric field strength is still considered insufficient to meet the heating requirements of approx. 1 MV/m for an industrial false-twist texturing process. It should be noted that this is only a very local, punctual fitness value. The yarn passes through several points of high field strength, and the generated heat will accumulate in the material. On the other hand, thermal losses to the surrounding air must be taken into account. The research hypothesis could not yet be fully validated, as the optimisation workflow has not yet identified an unconventional geometry that yields an electric field strength greater than 1 MV/m, which is sufficient to heat the PET yarn beyond 190 °C.

Several directions for future research can be identified. First, the geometric diversity of the resonator could be further increased at the cost of greater computational resource consumption by increasing the density of control points in the surface-contour representation and by adopting a slice-based parametrisation approach to introduce another degree of freedom along the axial direction of the cavity.

Second, future work could extend the optimisation formulation beyond a single-objective criterion. In addition to maximising the peak electric field strength at a single point, additional performance metrics, such as heating uniformity or reflected power, could be incorporated into a multi-objective optimisation framework. These additional metrics would enable a more comprehensive assessment of resonator performance under practical constraints. Other optimisation algorithms, in addition to the genetic algorithm, may also be explored.

Third, a multiphysics analysis and simulation approach that couples electromagnetic and thermodynamic effects should be explored. This approach would enable a deeper understanding of the temperature distribution within the yarn, minimising the sim-to-real gap for industrial applications.

Last but not least, construction restrictions need to be taken into account. Processes like welding, screwing, drilling, milling or 3D printing can only achieve certain geometries, so the optimal solution the algorithm determines might not be feasible to manufacture when those constraints are disregarded. Once a resonator cavity has been manufactured, the simulation needs to be validated by determining the resonator's unloaded Q-factor and by applying the prototype in the false-twist texturing process.

Funding: We thank the Federal Ministry of Research, Technology and Space for funding the research project *MicroHeatTex* through the funding guideline *KMU-innovativ: Energieeffizienz, Klimaschutz und Klimaanpassung* under the grant number 01LY2306.

With funding from the:
Federal Ministry of Research, Technology and Space

Use of LLMs and AI: In this work, Google Gemini was used in part for text translation, and editing was conducted with the help of Grammarly.

Conflicts of Interest: The authors declare no conflict of interest. The funders had no role in the design of the study; in the collection, analyses, or interpretation of data; in the writing of the manuscript, or in the decision to publish the results.

References

1. The Fiber Year GmbH. *The Fiber Year 2024*: *World Survey on Textiles & Nonwovens*, Roggwil, Schweiz, 2024.
2. Ortega, M.; Saynisch, A.; Yurtseven, B.-M.; Gries, T. A Review on False-Twist Texturing. *Fibers* **2024**, *12*, 36, doi:10.3390/fib12040036.
3. Oerlikon Barmag. *Exploring Draw Texturized Yarn (DTY)*: *A Comprehensive Guide*, Remscheid, 2023. Available online: https://www.oerlikon.com/en/industries/polymer-processing/exploring-draw-texturized-yarn-dty-a-comprehensive-guide/?mtm_source=linkedin&mtm_campaign=innovation-research-development-drive&mtm_medium=organic&mtm_group=oerlikon-marketing (accessed on 17 July 2023).
4. Dulmalik; Chafidz, A.; Fernandi, R.; Ardianto. Partially Oriented Yarn (POY) produced from semi-dull via melting spun using an extruder: Effect of die extruder temperature on elongation of the POY. *J. Phys.: Conf. Ser.* **2019**, *1295*, 12010, doi:10.1088/1742-6596/1295/1/012010.

5. Gries, T.; Veit, D.; Wulfhorst, B. *Textile technology*: *An introduction*, 2nd ed.; Hanser: Munich, Cincinnati, Ohio, 2015, ISBN 1569905657.
6. Veit, D. Einstellung von Falschdraht-Texturiermaschinen mit Hilfe der Evolutionsstrategie und neuronaler Netze. Dissertation; RWTH Aachen, 1999.
7. Olbrich, A. Analyse und Simulation der Drallerteilung durch Friktion zur Optimierung der Falschdraht-Texturierung. Dissertation; RWTH Aachen, 1995.
8. Jungbecker, P. *Expert interview with Dr.-Ing. Philip Jungbecker, Senior Manager Technology Texturizing Machines at Oerlikon Textile GmbH & Co. KG, Remscheid, Germany, conducted by Mathias Ortega on April 8, 2022*, Remscheid, 2022.
9. Rahbar, R.S.; Mojtahedi, M.; Maroufi, M.; Masoudian, Z. Effect of Yarn Wetting on Some Physical Properties of Polyamide 6 False-Twist Textured Yarn. *Research Journal of Textile and Apparel* **2010**, *14*, 75–81, doi:10.1108/RJTA-14-01-2010-B008.
10. Schmenk, B. Sicherung von Prozessstabilität und Garnqualität in der Falschdraht-Texturierung. Dissertation; RWTH Aachen, 2003.
11. Fourné, F. *Synthetic Fibers*: *Machines and Equipment, Manufacture, Properties Handbook for Plant Engineering, Machine Design, and Operation;* Hanser, München, 1999, ISBN 3-446-16072-8.
12. Atkinson, C. *False twist textured yarns*: *Principles, processes and applications;* Woodhead Publishing Limited: Oxford, 2012, ISBN 978-0-85709-559-6.
13. Canoglu, S. Effect of First Heater Temperature Variations on the Polyester Yarn Properties of False - Twist Texturing Techniques. *FIBRES & TEXTILES in Eastern Europe* **2009**, *17*, 35–39.
14. Finlayson, D.; Happey, F. Manufacture of artificial materials. E.P. 424,880, June 2, 1933.
15. Heberlein & Co. AG. Verfahren zur Herstellung wolleähnlicher Kunstseide. H 13100 VII/29a, March 11, 1932.
16. Hearle, J.W.S.; Hollick, L.; Wilson, D.K. *Yarn texturing technology;* CRC Press; Woodhead Pub: Boca Raton, Cambridge England, 2001, ISBN 0849313104.
17. Bruske, J.F. Beitrag zur Steigerung von Leistung und Qualität in der FD-Texturierung: Dissertation; RWTH Aachen, 1990.
18. Atkinson, C.; Spahlinger, P.; Fischer-Fürwentsches. Temcooler: direct active yarn cooling in draw-texturing. *Chemical Fibers International* **2005**, *55*, 105–108.
19. Meier, K. Verkürzung der Heizzone beim Falschdraht-Texturieren: Dissertation; RWTH Aachen, 1993.
20. Eskin, N. Analysis of a high temperature heater in a false twist texturing process. *Energy Conversion and Management* **2003**, *44*, 2531–2547, doi:10.1016/S0196-8904(03)00014-1.
21. BMWi Bundesministerium für Wirtschaft und Energie. *Energieeffizienz in Zahlen*: *Entwicklungen und Trends in Deutschland 2018*, Berlin, 2018.
22. Federal Ministry for the Environment, Climate Action, Nature Conservation and Nuclear Safety. Klimaschutzplan 2050: Klimaschutzpolitische Grundsätze und Ziele der Bundesregierung. Available online: https://www.bundeswirtschaftsministerium.de/Redaktion/DE/Publikationen/Industrie/klimaschutzplan-2050.pdf?__blob=publicationFile&v=1 (accessed on 24 February 2026).
23. Deutscher Bundestag. *Bundes-Klimaanpassungsgesetz (KAnG)*, 2023. Available online: https://www.recht.bund.de/bgbl/1/2023/393/VO (accessed on 24 February 2026).

24. United Nations. *Transforming our World: The 2030 Agenda for Sustainable Development*, New York City, NY, USA, 2015. Available online: https://sdgs.un.org/sites/default/files/publications/21252030%20Agenda%20for%20Sustainable%20Development%20web.pdf (accessed on 24 February 2026).
25. Graf, M.H. Grundlagen und Verfahren zur profilierten Erwärmung von PET-Preforms mit Mikrowellen. Dissertation; KIT, 2018.
26. Elshemy, N.S.; Haggag, K. New Trend in Textile Coloration Using Microwave irradiation. *Journal of Textiles, Coloration and Polymer Science* **2019**, *16*, 33–48, doi:10.21608/jtcps.2019.9928.1019.
27. Chao, H.-W.; Hsu, H.-C.; Chen, Y.-R.; Chang, T.-H. Characterizing the dielectric properties of carbon fiber at different processing stages. *Sci. Rep.* **2021**, *11*, 17475, doi:10.1038/s41598-021-96949-6.
28. Hashem, M.; Taleb, M.A.; El-Shall, F.N.; Haggag, K. New prospects in pretreatment of cotton fabrics using microwave heating. *Carbohydr. Polym.* **2014**, *103*, 385–391, doi:10.1016/j.carbpol.2013.11.064.
29. Bhat, N.V.; Kale, M.J.; Gore, A.V.G. Microwave Radiations for Heat-Setting of Polyester Fibers. *Journal of Engineered Fibers and Fabrics* **2009**, *4*, doi:10.1177/155892500900400402.
30. Veronesi, P.; Colombini, E.; Salvatori, D.; Catauro, M.; Leonelli, C. Microwave Processing of PET Using Solid-State Microwave Generators. *Macromol. Symp.* **2021**, *395*, 2000204, doi:10.1002/masy.202000204.
31. Savic, M.; Trajkovic, D.; Stojanovic, P.; Stepanovic, J. The influence of the variation of texturing process parameters on structural characteristics of polyamide textured yarns in the false twist. *Adv techn* **2016**, *5*, 64–72, doi:10.5937/savteh1602064S.
32. Taghavi Deilamani, M.; Rashidi, A.; Yazdanshenas, M.E.; Moghadam, M.B.; Eskandarnejad, S. Statistical Investigation of the Effect of Major Parameters of False Twist Texturing on the Dyeing Characteristic and Color Properties of Microfilament Polyester Yarn. *Moroccan Journal of Chemistry* **2022**, *10*, 160–179.
33. Veit, D. *Fibers*: *History, Production, Properties, Market*, 1st ed.; Springer International Publishing; Imprint Springer: Cham, 2022, ISBN 978-3-031-15308-2.
34. Li, Z.; Peng, K.; Ji, N.; Zhang, W.; Tian, W.; Gao, Z. Advanced mechanisms and applications of microwave-assisted synthesis of carbon-based materials: a brief review. *Nanoscale Adv.* **2025**, *7*, 419–432, doi:10.1039/d4na00701h.
35. Meloni, E.; Iervolino, G.; Palma, V. Basics of Microwave Heating and Recent Advances. In *Advances in Microwave-Assisted Heterogeneous Catalysis,* 1st ed.; Hu, J., Ed.; Royal Society of Chemistry The: La Vergne, 2024; pp 1–24, ISBN 978-1-83916-817-8.
36. *Advances in microwave and radio frequency processing*: *Report from the 8th International Conference on Microwave and High Frequency Heating held in Bayreuth, Germany, September 3-7, 2001;* Willert-Porada, M., Ed.; Springer Berlin Heidelberg: Berlin, Heidelberg, 2006, ISBN 3-540-43252-3.
37. Ember. Electricity Data Explorer. Available online: https://ember-energy.org/data/electricity-data-explorer/ (accessed on 1 April 2026).
38. Metaxas, A.C.; Meredith, R. *Industrial microwave heating*, Reprinted.; The Institution of Engineering and Technology: London, 2008, ISBN 9780906048894.
39. Metaxas, A.C. *Foundations of electroheat*: *A unified approach;* Wiley: Chichester, 1996, ISBN 9780471956440.

40. Graf, M.; Räuchle, E.; Urban, H.; Kaiser, M.; Alberts, L.; Emmerich, R.; Elsner, P. FEM-Simulation von Mikrowellenfeldern für die Entwicklung von Mikrowellen- und Plasmaanlagen. *Chemie Ingenieur Technik* **2005**, *77*, 338–342, doi:10.1002/cite.200590028.
41. Yoshikawa, N. Mechanism of Microwave Heating of Matter. In *RF Power Semiconductor Generator Application in Heating and Energy Utilization*; Horikoshi, S., Serpone, N., Eds.; Springer Singapore: Singapore, 2020; pp 71–89, ISBN 978-981-15-3547-5.
42. Zorn, R. Logarithmic moments of relaxation time distributions. *The Journal of Chemical Physics* **2002**, *116*, 3204–3209, doi:10.1063/1.1446035.
43. Havriliak, S.; Negami, S. A complex plane representation of dielectric and mechanical relaxation processes in some polymers. *Polymer* **1967**, *8*, 161–210, doi:10.1016/0032-3861(67)90021-3.
44. Zhang, S.; Qiu, Q.; Zeng, C.; Paik, K.-W.; He, P.; Zhang, S. A review on heating mechanism, materials and heating parameters of microwave hybrid heated joining technique. *Journal of Manufacturing Processes* **2024**, *116*, 176–191, doi:10.1016/j.jmapro.2024.02.055.
45. Jensen, E. Cavity basics. *Yellow Report CERN-2011-007* **2011**, 259-275.
46. Zinke, O.; Brunswig, H. *Hochfrequenztechnik 1*: *Hochfrequenzfilter, Leitungen, Antennen*, 5., neubearbeitete Auflage; Springer Berlin Heidelberg: Berlin, Heidelberg, s.l., 1995, ISBN 978-3-662-00813-3.
47. Everything RF. WR159 | WG13 | R58 - Rectangular Waveguide WR159 | WG13 | R58 - Rectangular Waveguide Size: WR159 Specifications. Available online: https://www.everythingrf.com/tech-resources/waveguides-sizes/wr159 (accessed on 8 April 2026).
48. Rani, R.; Jain, S.; Garg, H. A review of nature-inspired algorithms on single-objective optimization problems from 2019 to 2023. *Artif Intell Rev* **2024**, *57*, doi:10.1007/s10462-024-10747-w.
49. Bisht, D.C.S.; Ram, M. *Computational Intelligence*: *Theoretical Advances and Advanced Applications*, 1st ed.; Walter de Gruyter GmbH: Berlin/Boston, 2020, ISBN 9783110671353.
50. Albadr, M.A.; Tiun, S.; Ayob, M.; AL-Dhief, F. Genetic Algorithm Based on Natural Selection Theory for Optimization Problems. *Symmetry* **2020**, *12*, 1758, doi:10.3390/sym12111758.
51. Forrest, S. Genetic algorithms: principles of natural selection applied to computation. *Science* **1993**, *261*, 872–878, doi:10.1126/science.8346439.
52. Gen, M.; Cheng, R. *Genetic algorithms and engineering design;* Wiley: New York, Weinheim, 1997, ISBN 9780471127413.
53. Whiting, E.B.; Campbell, S.D.; Kang, L.; Werner, D.H. Meta-atom library generation via an efficient multi-objective shape optimization method. *Opt. Express* **2020**, *28*, 24229–24242, doi:10.1364/OE.398332.
54. Whiting, E.B.; Campbell, S.D.; Mackertich-Sengerdy, G.; Werner, D.H. Dielectric Resonator Antenna Geometry-Dependent Performance Tradeoffs. *IEEE Open J. Antennas Propag.* **2021**, *2*, 14–21, doi:10.1109/OJAP.2020.3037826.
55. van Rossum, G. *Python tutorial*, Amsterdam, The Netherlands, 1995.
56. Python Software Foundation. python (TM): Python is a programming language that lets you work quickly and integrate systems more effectively. (accessed on 8 April 2026).
57. Ansys, Inc. Ansys HFSS: Best-In-Class 3D High Frequency Structure Simulation Software. Available online: https://www.ansys.com/products/electronics/ansys-hfss (accessed on 30 June 2026).
58. Everything RF. WR430 | WG8 | R22 - Rectangular Waveguide Size: WR430 Specifications. Available online: https://www.everythingrf.com/tech-resources/waveguides-sizes/wr430 (accessed on 8 July 2026).